

Contents

1 Deep Radiomics for histological grade prediction	1
1.1 Introduction	1
1.2 Histological HCC grade in the literature	1
1.2.1 Histological HCC grading systems	1
1.2.2 DLR based study to predict the histological HCC grade	5
1.3 Experimental workflow	6
1.3.1 Registration	7
1.3.2 TCIA-dB unsupervised liver segmentation	7
1.3.3 TCIA-dB ANTs registration	9
1.3.4 TCIA-dB unsupervised multiphase tumor segmentation	10
1.3.5 Prediction of the histological grade on TCIA-dB	14

1 Deep Radiomics for histological grade prediction

1.1 Introduction

So far, we proved that semantic segmentation of liver tissues can be performed using DL through robust CV training on both **3DIrcad-dB** and **TheraHCC-dB**.

We also demonstrated that both a cascaded architecture and the use of multiphase information allows a better segmentation accuracy than using single phase images only.

One of the main goals of our research work was to use imaging features to predict pathological behavior of the disease. The prediction of the histological grade of the tumor was rarely studied, since only one study used deep learning tools to perform this task but with MR images as input [1]. Indeed, this task appears to be more challenging than previous DLR liver-related work where either the type of FFL or the treatment response (such as the recurrence) were predicted (**see DLR section**).

1.2 Histological HCC grade in the literature

1.2.1 Histological HCC grading systems

Several types of histological grading systems exist, with the most frequent ones being ES 1954 (Edmonson-Steiner) [2] and WHO 2010 (World Health Organization) [3]. Differences between these two grading systems are given in the figure 1.

Reference	Grades	Architecture	Cytology	Other features
World Health Organization (21)	Well differentiated	Thin trabecular, frequent acinar structures	Minimal atypia	Fatty change is frequent
	Moderately differentiated	Trabecular (3 or more cells in thickness) and acinar	Abundant eosinophilic cytoplasm, round nuclei with distinct nucleoli	Bile or proteinaceous fluid within acini
	Poorly differentiated	Solid	Moderate to marked pleomorphism	Absence of sinusoid-like blood spaces
	Undifferentiated	Solid	Little cytoplasm, spindle, or round-shaped cells	—
Edmondson and Steiner (13)	Grade I	—	—	Areas of carcinoma where distinction from hyperplastic liver is difficult
	Grade II	Trabecular, frequent acini (lumen varying from tiny canalicular to large thyroid-like spaces)	Resemblance to normal hepatic cells; larger nuclei; abundant acidophilic cytoplasm	Cell borders sharp and clear cut; acini containing bile or protein precipitate
	Grade III	Distortion of trabecular structure, acini less frequent than grade II	Larger, more hyperchromatic nuclei, granular but less acidophilic cytoplasm	Acini are less frequent; tumor giant cells may be numerous
	Grade IV	Medullary, less trabeculae, rare acini	Highly hyperchromatic nuclei, scanty cytoplasm, with fewer granules	Loss of cell cohesiveness; giant, spindle or short-plump cells can be found

Figure 1: Features differences between the WHO and the ES1954 histological grading systems as detailed by Martins et al. [4] ©2017 Martins-Filho, Paiva, Azevedo and Alves

Even if ES 1954 is the most widely used grading system, a lot of divergences in the assessment of the grade can be found in the different studies reviewed by Martins et al. [4].

The organization of the patients in different numbers of tiers (3 or 4) G1, G2, G3 and potentially G4, and the possible classification into low or high differentiation level reveals a high variability in the assessment of the histological grade, as seen in the figure 2. As an example, some studies suggested that G2 is closer to G1 than to G3 [5, 6], therefore, a classification that separates both G1 and G2 in one group and G3 (with potentially G4 if available) in the other can be understood.

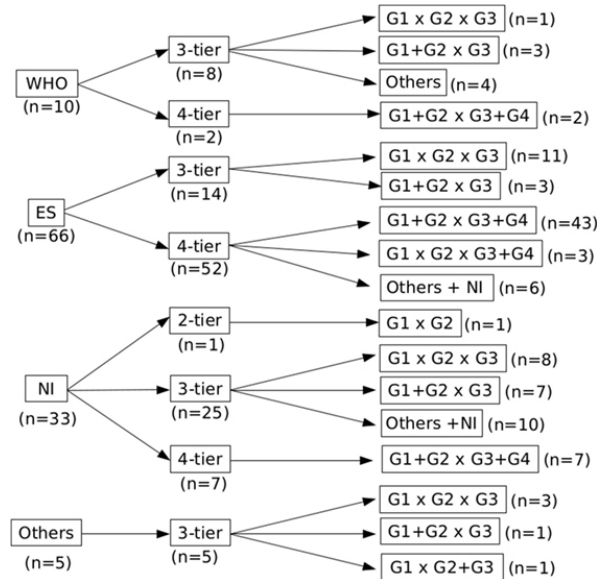


Figure 2: Distribution of the studies according to the grading reference, number of tiers, and data analysis, as detailed by Martins et al. [4] ©2017 Martins-Filho, Paiva, Azevedo and Alves

This difference in the classification of the patients was also noticed by Han et al. [5] and detailed in

the figure 3. They reviewed different articles that used the histological grade to predict the prognostic of the patients, and realized that no clear guidelines were given for tumor presenting regions with heterogeneous grades (two examples of heterogeneous histological HCC slices are given in the figure 4).

Table 3 Studies related to histologic differentiation of hepatocellular carcinoma

Author	Definition of heterogeneous histologic grades	Comparison of histologic grades	Clinical significance of histologic grades
Chou	None	G1 vs G2 vs G3 vs G4	Higher histologic grades were more prevalent in microvascular invasion in HCC
Lim	None	G1 vs G2 vs G3	Up-regulation of Notch1 by p53 with Snail up-regulation promotes invasiveness of HCC and increases higher histologic grades
Decaens	None	G1 vs G2 vs G3	Histologic grades of HCC can be used as the new score for patient selection for liver transplantation
Pirisi	None	G1 & G2 vs G3	Histologic grades of HCC are usually underestimated in core biopsy
Zhou	None	G1 & G2 vs G3 & G4	Histologic grading could raise the predictive efficiency of TNM stage for survival of patients with HCC after liver resection
Pawlak	Poorest	G1, G2 & G3 vs G4	Selection of candidates for liver transplantation based on needle core biopsy tumor grade may be misleading
Minagawa	None	G1 vs G2, G3 & G4	On multivariate analysis, well-differentiated HCC is a good prognostic factor for patients with HCC after liver resection
Kim	Predominating	G1 vs G2 vs G3	Higher histologic grades might decrease cancer-free survival rate after radiofrequency ablation for HCC patients
Pawlak	None	G1 & G2 vs G3 & G4	On univariate analysis, higher histologic grade was a significant predictor of survival after hepatectomy for patients with major portal or hepatic vein invasion
Pawlak	Poorest	G1 vs G2 vs G3 & G4	A higher histologic grade can predict occult vascular invasion in HCC larger than 5 cm
Carlisi	None	G1 & G2 vs G3	Histologic grade is one predictor of HCC recurrence after liver transplantation

HCC, hepatocellular carcinoma.

Figure 3: Classification groups used by the studies reviewed by ©Han et al. [5]

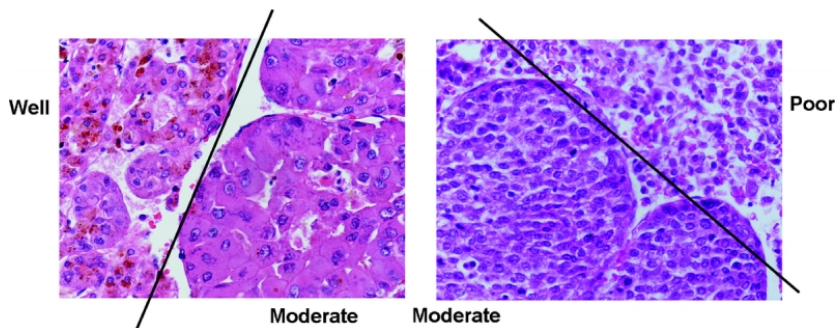


Figure 4: Examples of heterogeneous histological slices, as depicted by Pawlik et al. [7] ©2007

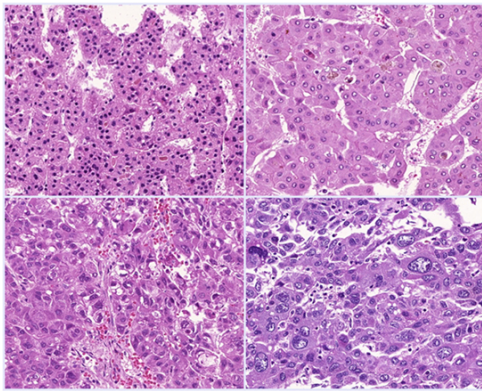
Lippincott Williams & Wilkins, Inc

The two possible solutions were to consider the worst grade (as recommended by the ES grading system), or to consider the most present one (recommended by the WHO grading system), however clear explanations of the decision taken in such cases are often undisclosed in the different studies.

The question regarding which histological HCCs grading system to use remains open. Moreover, various teams proposed to introduce a more complete grading system where the different features are classified separately as suggested by Martins et al. and depicted in the figure 5.

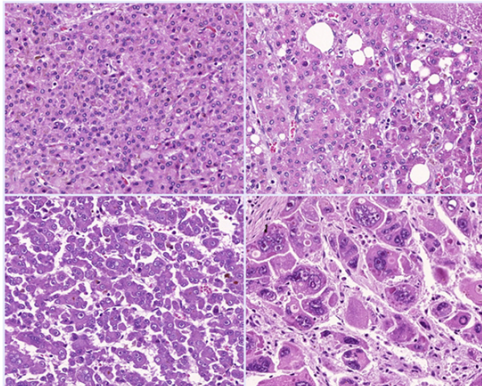
It is common to differentiate between the *clinical* and the *pathological* grade, where the *clinical* one corresponds to the assessment performed preoperatively, and the *pathological*¹ one corresponds to the

¹Important to distinguish from the pathological stage which mainly corresponds to the TNM.



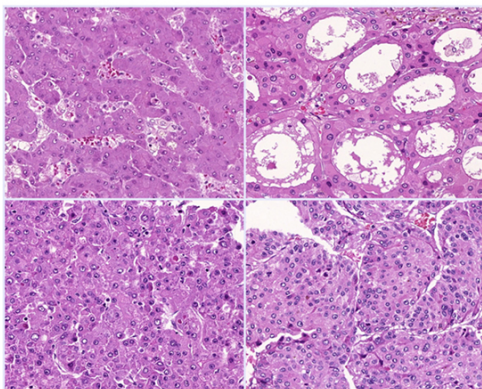
Nuclear Grade:

- Grade I: Homogeneous, near-normal nuclei;
- Grade II: mild pleomorphism;
- Grade III: moderate pleomorphism, irregular distribution of chromatin;
- Grade IV: marked pleomorphism, bizarre nuclei.



Nucleolar Grade (similar to Fuhrman's):

- Grade I: nucleoli barely seen at 400x;
- Grade II: evident nucleoli at 100-200x;
- Grade III: large nucleoli, visible at 100x;
- Grade IV: prominent nucleoli at 40x.



Architectural Grade:

- Grade I: trabecular, 2-3 cells wide;
- Grade II: pseudoglandular pattern;
- Grade III: mid-trabecular (4-10 cells wide);
- Grade IV: macrotrabecular (> 10 cells wide) or solid/bizarre patterns.

Figure 5: New histological HCC grading system proposed by ©Martins et al. [4]

evaluation of the sample collected during the surgery.

Some studies even suggested that the preoperative histological grade is not accurate enough to be used as a prognostic factor, and that because of the high difference between the NCB (needle core biopsy) grade and the one obtained from the final surgical specimen (resulted from the analysis of samples collected during surgery). Pawlik et al. exposed the concordance in estimating both the clinical and the pathological grades, their results were detailed in the figure 6.

As a conclusion, the problem regarding the histological classification of HCC remains open. Two standards are widely used, namely the ES one from 1954 and the WHO from 2010. They both initially contain 4 groups, but differ in the features to consider and the way heterogeneous lesions are supposed

TABLE 3. Concordance of Tumor Grade on Preoperative Needle Core Biopsy Versus Final Surgical Pathology Using 3-Tier Grading System (κ statistic = 0.18)

Preop. Needle Biopsy	Final Surgical Pathology			Total
	Well	Moderate	Poor	
Well	17	14	4	35
Moderate	15	16	13	44
Poor	2	3	9	14
Total	34	33	26	93

Figure 6: Concordance of pathological and clinical tumor grade estimation, as detailed by Pawlik et al.

© 2007 Lippincott Williams & Wilkins, Inc. [7]

to be classified. When different grades are encountered in the lesion specimen, ES 1954 recommends to consider the worst one, whereas WHO 2010 advices to consider the most frequent one. New grading systems were introduced lately in order to overcome these specific problems.

We will now focus on the only study in the literature that tackled the problem of predicting the histological grade of HCCs through a DL architecture with medical images, before presenting our own automatic DL pipeline.

1.2.2 DLR based study to predict the histological HCC grade

To our knowledge, only one study tackled the problem of estimating the histological grade of HCCs using a DL architecture, but with MR images as input [1].

Yang et al. incorporated 42 patients suffering from HCC in their study, resulting in a total of 51 HCCs. Each lesion was analyzed by 2 experienced pathologists who estimated their histological grade after microscopic examination (the lesions were classified as well, moderately and poorly differentiated, following the WHO classification system [3]). The extracted tissues were obtained through either biopsy (12 patients) or after surgical removal (2 liver transplants and 28 liver resection). All the 42 patients underwent pre-operative multiphasic MR imaging examinations and images were available at 5 different phases (precontrast, late arterial, portal venous, equilibrium and delayed phases). They obtained a dataset composed of 9 well, 7 poorly and 35 moderately differentiated HCCs.

For each patient, a ROI was placed by one expert at the maximal axial cross-sectional area to entirely cover the tumor. The ROI was copied in the 2 slices above and below the chosen one, to obtain a 3D volume. Intensities of each volume were normalized and 4D tensors were created for each patient so that each tensor had a $32 \times 32 \times 5 \times 5$ shape (32×32 corresponding to the resample axial ROI

dimension, the third dimension being the number of retained slices, and the last dimension being the dynamic temporal evolution of the ROI with the 5 phases).

The used architecture is depicted in the figure 7. It first splits the 4D tensors into 5 3D objects so that each slice is treated separately. Each 3D volume was then processed by 2 convolutional, 2 max pooling and 1 fully connected layer. The features of each slice were then concatenated, before a second fully connected layer followed by a dense layer with a softmax activation function outputs the probability of belonging to each one of the three classes (well, moderately or poorly differentiated).

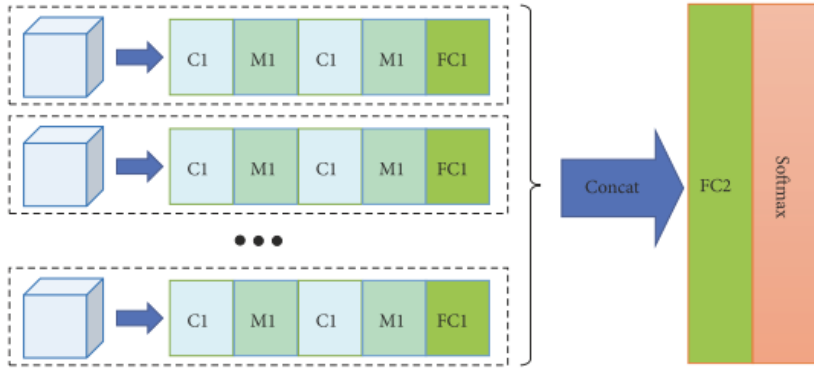


Figure 7: MCF-3DCNN architecture as detailed by ©Yang et al. [1]

During the training process, they implemented a label-shuffling method to overcome the problem of imbalance data. Furthermore, to avoid the effect of overfitting, they trained their network with augmented data (original images were transposed, rotated, and flipped), a learning rate reduction and the addition of dropout (rate = 0.5).

Using their architecture they were able to correctly classify the HCCs into the 3 differentiation groups with a mean accuracy of **74%**.

Their study however suffers from a lot of limitations such as the reduced size of the cohort, the imbalance data and the fact that the analysis was only performed in a manually drawn VOI.

We have decided to tackle the same issue, but we implemented a fully automatic pipeline where both the segmentation and the grade prediction steps were performed by DL networks.

1.3 Experimental workflow

TCIA-dB is the only open dataset where both tomographic images and histological grade ground truth are available. It originally only contained raw images without annotations, so an expert performed the delineations for both the tumor and the necrosis areas on PV images only.

In order to perform the prediction of the histological grade, our idea is to use the imaging features retained for the liver tissue segmentation, especially those used to segment tumoral structures.

We believe that one easy way to extract relevant imaging features is to use those retained by the semantic segmentation networks, thus the better the accuracy regarding the semantic segmentation of the liver tissues, the more accurate the histological grade prediction will be.

As explained previously, we proved that a cascaded architecture combined with the use of temporal contrast enhanced images allows a better delineation of liver tissues. It has been proven that using temporal information can improve the accuracy of the grade prediction, by exploiting the wash-in wash-out specific features [8].

To conduct our DLR study, we first performed a multiphasic semantic segmentation of the TCIA-dB, before predicting the histological grade.

To achieve a multiphasic semantic segmentation of the liver tissues we have to ensure that both the liver and its internal structures such as the potential tumors are located at the same spatial position between the different CECT volumes.

1.3.1 Registration

One way to perform a registration is to implement a series of transformations (rigid or non-rigid) that will match a moving volume to a target one. Each step of the registration is controlled by a similarity loss. When dealing with CT volumes the available losses controlling the different steps of the registration pipeline can be affected by areas of the body with a high gradient such as the bones for example. When registering two CT volumes, one can either directly use both the entire volumes or constraints the registration to a specific area (aka mask). The liver being a soft organ, it easily moves with the respiratory motions, in order to reduce the effect of the neighboring parts of the abdomen, we have decided to restrict the computation of the similarity metrics to the dilated liver mask area so that the registration algorithm mainly focus on the gradient present along its borders.

Consequently, the first step for the TCIA-dB registration is to perform a liver semantic segmentation (green arrows in the figure 8).

1.3.2 TCIA-dB unsupervised liver segmentation

In the available datasets ([ref table](#)), only TheraHCC-dB and LITS-dB contained expert liver delineation.

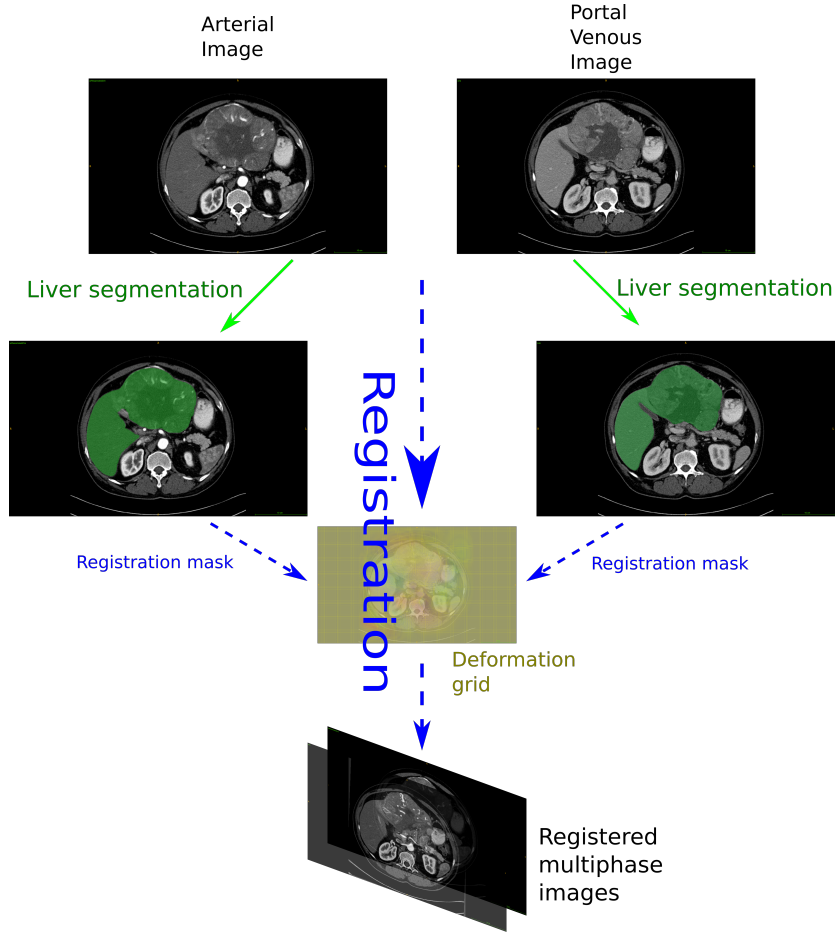


Figure 8: Illustration of the registration pipeline applied to the images of TCIA-dB. The first green arrows correspond to the liver segmentation using a network trained on the LITS-dB. Dashed blue arrows correspond to the ANTs registration pipeline, where a dilated version of the predicted liver annotations maps are used as registration masks. The ANTs algorithm implements 3 transformations: a rigid, an affine, and a diffeomorphic Syn transformation that computes a deformation grid [9]. The 3 steps of the ANTs call allows us to obtain registered multiphase images.

TheraHCC-dB contains annotations only on sparse slices across the liver, whereas LITS-dB contains full 3D pixel-wise liver annotation but it only contains monophase images, without any information regarding the acquisition phase (AR, PV and potentially DELAY volumes are mixed in the dataset). Our experiments however showed that a liver segmentation network trained on sufficiently enough cases is able to perform the semantic segmentation of both AR and PV raw images independently. We trained our network called **CECT-Liver** on the 131 volumes of the LITS-dB using the same hyperparameters as the ones detailed previously (See **Semantic segmentation applied to the study of HCC**). When testing the **CECT-Liver** network on TheraHCC-dB we obtained a mean slice-wise DSC of 90.4 ± 17.5 on the PV images and 86.9 ± 19.1 on the AR images. Those results, close to those obtained in our previous work using a CV approach [10], proved that **CECT-Liver** can perform liver segmentation on

both AR and PV unseen images.

The **CECT-Liver** network was also able to segment unseen volumes of the TCIA-dB in both AR and PV phases even when the liver presents a big lesion, as we can see in the figure 9.

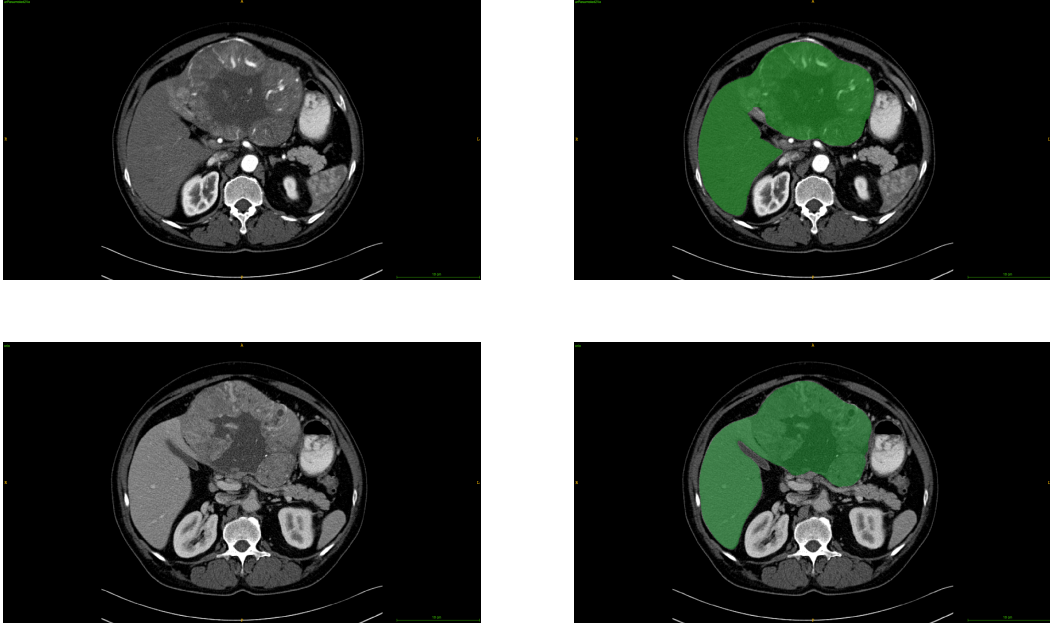


Figure 9: Example of liver segmentation using the **CECT-Liver** network on TCIA-dB patients (Top row AR images, bottom row: PV images, left: Raw images, right : liver segmentation as overlay).

Once a robust liver segmentation was obtained, we implemented our registration pipeline.

We have decided to implement the registration pipeline using ANTs [11], since it has already been used for liver CT scans registration [12, 13].

1.3.3 TCIA-dB ANTs registration

The classical ANTs registration pipeline is made of 3 steps. The first two steps consist of linear transformations, where a rigid transformation is first applied, followed by an affine transformation. The last one is generally non-linear. In our pipeline, we used a Syn (*Standard Symmetric normalisation*) transformation, which processes a gradient field, determining how each point of the space will shift [9].

The MI (Mutual Information) was used as loss function for the first two steps because it has the advantage of computing the similarity at a large scale. Linear transformations tend to roughly bring both volumes in the same space so we decided not to use a finer metric. For the Syn transform, we used the CC (Cross Correlation) as loss function. The CC has the advantage of looking precisely in a region around each voxel when computing the similarity between the two volumes.

During the registration process, the liver segmentation was used as registration mask, and we decided to set the PV volume as target (fixed) volume since it usually presents the finer voxel resolution when compared to AR (or DELAY) volume, and since it contains the original expert annotations.

1. We initially resampled the AR volume so it has the same resolution as the corresponding PV volume.
2. We performed the liver segmentation using **CECT-Liver** on both the PV and the resampled AR volumes in a slice-wise manner with a classical post-processing consisting in applying a binary opening operation to the mask and conserving the big connected component (see green arrows in the figure 8). We obtained a liver mask for both the PV and the resampled AR volumes.
3. We applied the registration using both dilated version of the two masks obtained at the end of the second step as registration masks (as depicted by the dashed blue arrows in the figure 8) (we dilated the liver mask with a SSE of 5cm when setting the registration mask in order to counter any error in the segmentation process, and to always have both the liver and its border included in the registration mask)
4. The registration allows us to obtain both a new registered arterial volume, a transformation matrix and a deformation field volume. In the axial plane, the obtained deformation fields tend to present high deformation at both the top and the bottom of the liver (which can be explained anatomically since they are surrounded by the air and will be more subject to deformation than central areas of the liver) whereas central areas of the liver present high deformation close to the border. Examples of obtained deformation fields at the end of the registration pipeline are depicted in the figure 10.

Table 1: Registration pipeline

One way to assess the precision of the registration is to apply the transformation matrix to the initial resampled AR liver mask and to compute the DSC with the target PV liver mask. When applying this evaluation, we obtained a mean patient-wise DSC of 92.8 ± 3.8 at the end of the registration step on the **TCIA-dB**, sufficient to consider the registration as successful when compared with obtained by state-of-the-art registration methods applied to the liver [12].

The complete registration pipeline applied to the **TCIA-dB** is detailed in the table 1.

1.3.4 TCIA-dB unsupervised multiphase tumor segmentation

Once both the AR and PV volumes of the **TCIA-dB** were registered, and the liver masks obtained, we built the second step of our cascaded architecture, dedicated to the multiphasic tumor segmentation.

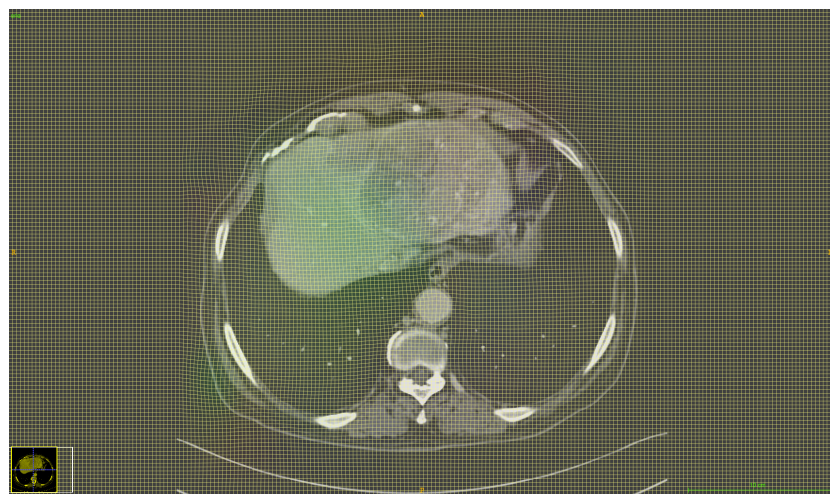
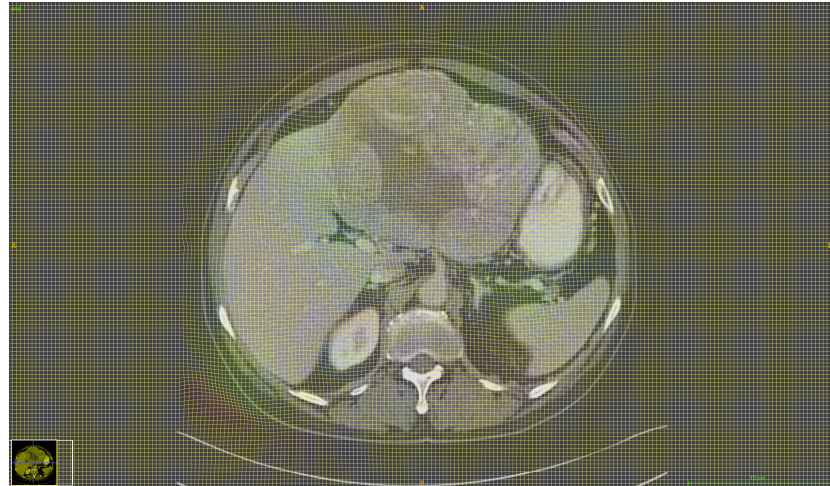


Figure 10: Example of deformation grids obtained after applying the registration pipeline on TCIA-dB patients

In order to train such a network, we created a multiphase (arterial and portal venous) database where the temporal volumes of a given patient are registered and where segmentations of both the liver and tumor regions are available. TheraHCC-dB and G-dB were the only two datasets containing multiphasic images (as we can see in the [dataset table](#), however G-dB initially contained ground truth annotation only for the tumors, with segmentations performed only on the AR phase images. Since G-dB contains more cases than TheraHCC-dB, we have decided to build our multiphasic tumor segmentation network on this dataset. However in order to train a tumor segmentation network, our cascaded architecture requires to have the liver segmentation mask as input for the second step (as depicted in the figure [ref figure Cascade CARS](#)), therefore we had to obtain the liver segmentation mask for the patients of the G-dB.

AR and PV volumes of the G-dB dataset were initially not registered so we applied the same registration pipeline as the one used for TCIA-dB (see table 1). After applied the procedure to each patient of G-dB, we used the resulting transformation matrix to transform the AR tumor mask to the PV space as depicted by the red and green dashed arrows in the figure 11.

We then fused the liver and the tumor masks to obtain a multiclass segmentation mask that can fit both the PV and the registered AR volumes, as depicted in the figure 12.

We were able thanks to our cascaded architecture and a robust liver segmentation network to enhance the volumes present in G-dB that originally contained only experts annotations for the tumor area on AR volumes.

Once a complete database where both the liver and the tumor segmentation masks were available, and where AR and PV volumes were registered, we trained a robust multiphase tumor segmentation network.

We trained both a **DMP-Tumor** and a **MPF-Tumor** segmentation network on the registered G-dB dataset, and evaluated them on TCIA-dB which contained expert tumor annotations. We evaluated both **DMP** and **MPF** architectures since no statistical differences were available when comparing results obtained for the tumor segmentation in our previous work on TheraHCC-dB [10].

After training both architectures with the same parameters, we obtained a mean patient-wise DSC of 73.2 ± 20.6 with **MPF** architecture versus 64.9 ± 27.2 when using the **DMP** when evaluating the models on the TCIA-dB patients. An example of prediction on the TCIA-dB is depicted in the figure 13.

Those results obtained on an external dataset tend to show the precision of the tumor segmentation when training a cascaded architecture with a sufficient number of cases. We retained the **MPF-Tumor** segmentation network since it performed significantly better than the **DMP** one ($p = 0.02$ using a

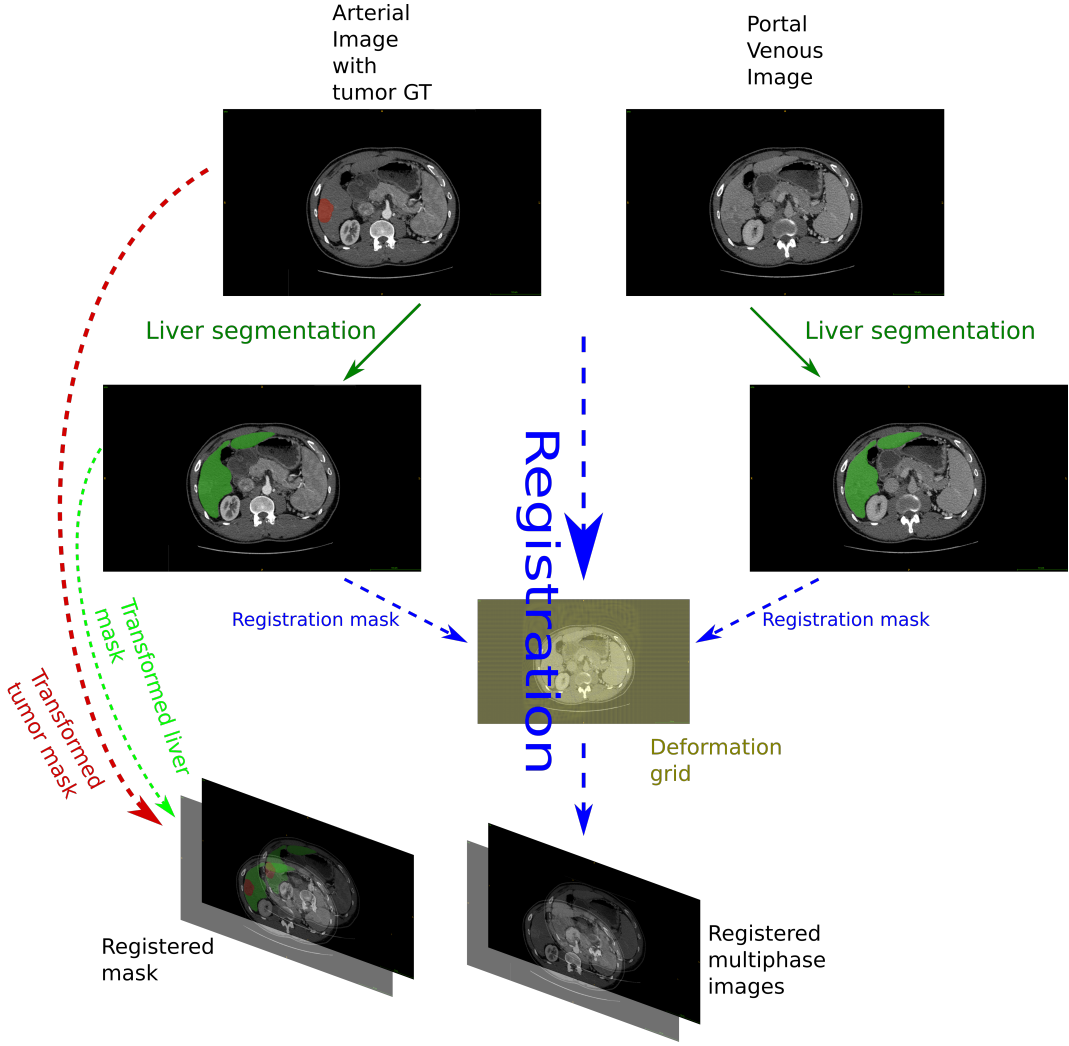


Figure 11: Illustration of the registration pipeline applied to G-dB. A similar approach as the one applied to TCIA-dB is performed to obtain the registered multiphase images. A final step is added here to transform both the tumor and the liver masks using the registration transformation matrix (red and green dashed arrows)

Wilcoxon signed paired rank test on the patient-wise DSC). We confirmed the benefit of the cascaded architecture since those results were obtained using an architecture where the first network was trained on LITS-dB and the second on G-dB. We were also able to use a monophase network for the first step and a multiphasic network for the second. This work proved the ability of deep learning (semantic segmentation network) combined with image processing (registration) to enhance and complete weakly annotated databases (both TCIA-dB and G-dB were enhanced in the same way).

Finally, we decided to keep only two stages in our cascaded architecture since the only available dataset with expert necrosis annotation was the TheraHCC-dB, containing only 7 patients. This small amount of cases combined with the design of TheraHCC-dB (only sparse slices are annotated across the volume) might not be enough to precisely differentiate between the active and the necrotic part of the lesions

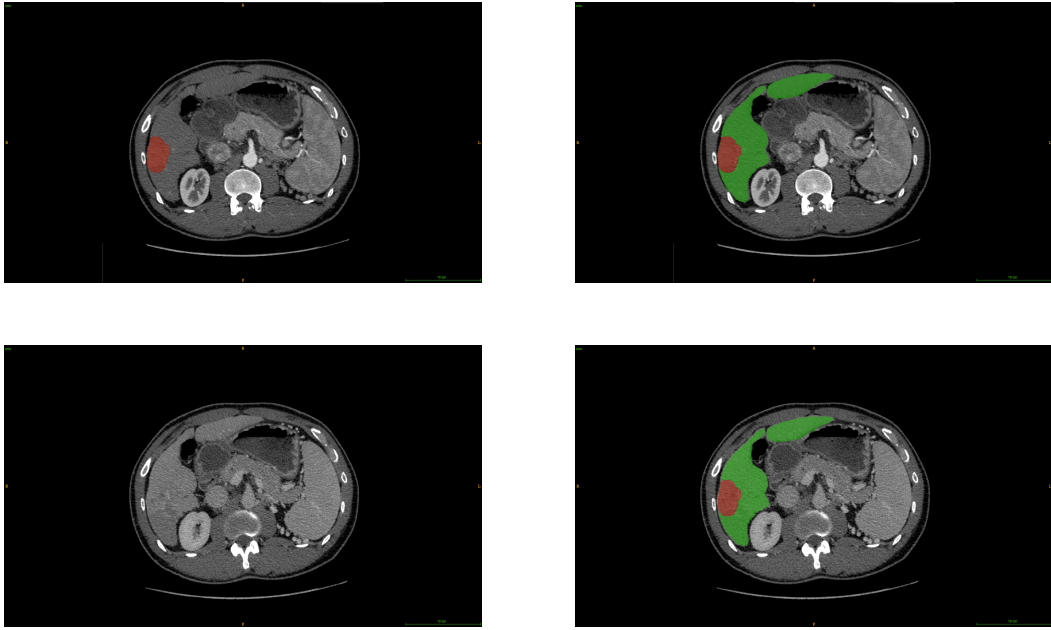


Figure 12: Example of a patient from G-dB, obtained after enhancing the dataset with our semantic segmentation network and our registration pipeline. Top row: AR_registered volume with original tumor expert segmentation, bottom row: PV_volume, left: original raw volumes, right: segmentation mask overlay where the parenchyma is obtained through our segmentation pipeline and the tumor was initially delineated by an expert then transformed to fit the target volume space.

on unseen cases. Moreover, the necrosis segmentation appears to be more sensitive than the tumor segmentation, especially because the necrosis requires separate annotations in each phase (in case of AR and PV volumes) since necrotic tissues will respond differently to the evolution of contrast medium.

1.3.5 Prediction of the histological grade on TCIA-dB

After obtaining the final cascaded architecture, we built our network responsible for the histological grade prediction.



Figure 13: **TODO: change the figure to better see the differences** Example of an image from the TCIA-dB, with the obtained predicted tumor segmentation using the **MPF-Tumor** segmentation network (left: raw, Middle: expert annotation, right: obtained segmentation)

TCIA-dB contains images from 18 patients, where 9 were diagnosed with a grade 3 (G3), 7 with a grade 2 (G2) and 2 with a grade 1 (G1). In order to obtain a balanced training dataset, it has been decided to split them into two groups, the first containing G1 and G2 patients, and the second containing G3 patients, as it has been done previously in the literature since G2 was considered as being closer to G1 than to G3 [5, 6]. Patients from the first group (G1 and G2) were considered as having a low grade (LG), whereas those from the second group have a high grade (HG). As explained previously, to train a network dedicated to predict the histological grade, we have decided to focus on what we called the relevant imaging semantic features. We therefore extracted the features from the second network of our cascaded architecture, to focus on the temporal behavior of the tumor.

The retained network (**MPF-Tumor** architecture **as depicted previously**) is made of 2 classical U-Net networks, where each one of them takes either the AR or the PV image as input. We believe that the compressed information present in the bottleneck part of the network can be sufficient to encode the total information present in the image (the U-Net will work as an auto-encoder for the semantic information). Therefore, we extracted for each patient of the TCIA-dB, this encoded information in a slice-wise manner, represented by two $32 \times 32 \times 512$ features cubes (one per phase in the **MPF-Tumor** architecture) per slice as depicted in the figure 14.

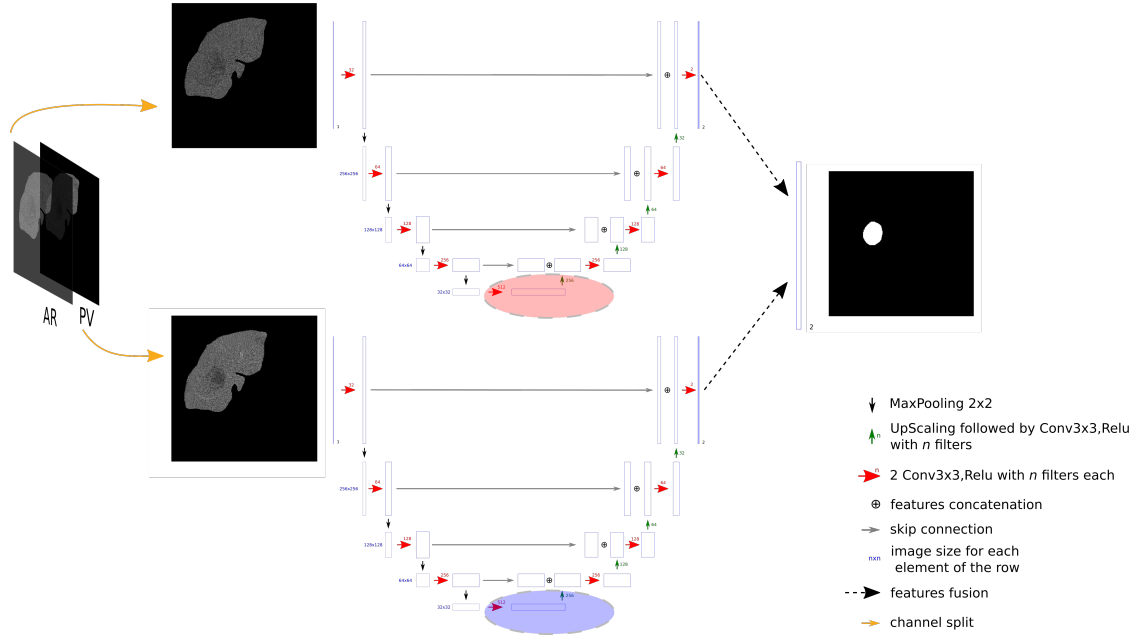


Figure 14: Red and blue areas correspond to the bottleneck part of the U-Net network where the features extraction is performed. Each image is then represented as a $32 \times 32 \times 512$ features cube.

Before applying the extraction of the features, we normalized the dimension of the different volumes of the dataset, so that each voxel measures $0.68 \times 0.68\text{mm}$ in the axial plane (because it corresponds to the resolution of the images used to train our semantic segmentation network), and that the volumes

have a 2.5mm z-spacing (corresponding to the spacing of the majority of the PV volumes in TCIA-dB).

We finally built an architecture responsible for the grade prediction. We focused only on the centrally located tumor slices, since the histological grade corresponds to a measurement of the evolution of the disease, which tends to have more physiological effects at the center of the tumor. Centrally located slices will therefore exhibit the highest grade for a given patient.

Therefore, a slice-wise architecture was built, first because the features were computed in a slice-wise manner and second because the histological grade tends to be heterogeneous in the lesion, meaning that a slice-wise approach allows us to give a finer prediction to find potential areas with a more advanced disease.

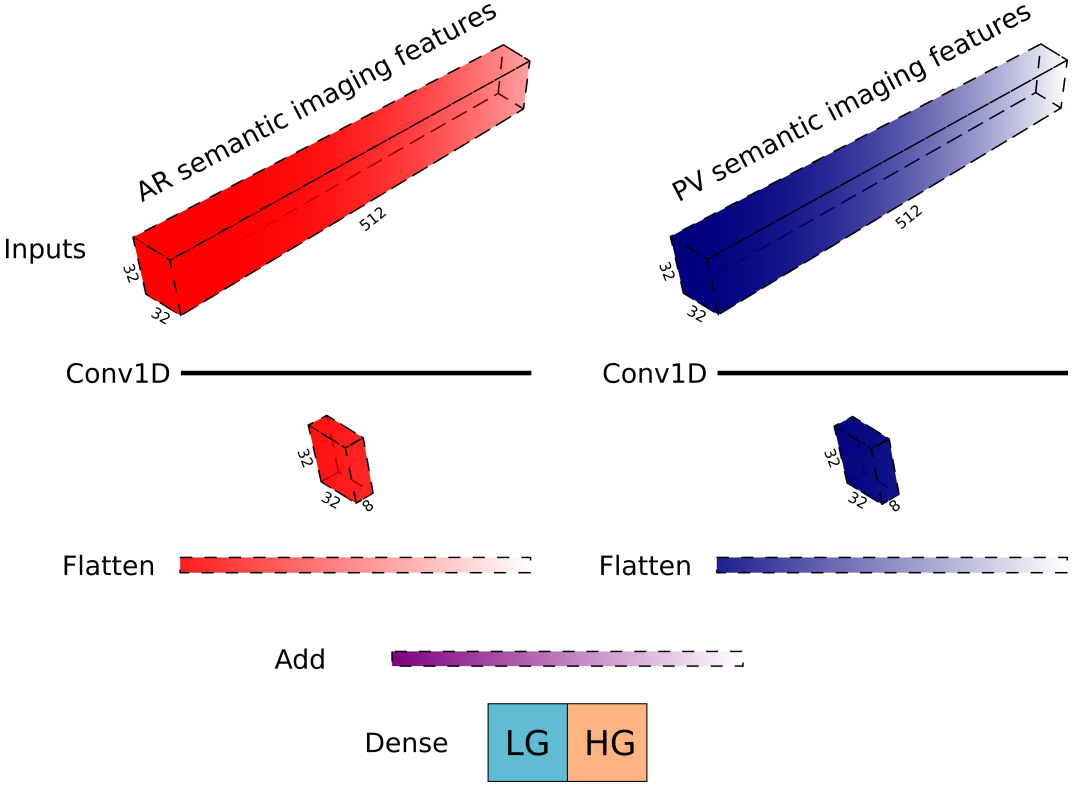


Figure 15: Slice-wise histological grade prediction using both AR and PV retained semantic imaging features

The architecture depicted in the figure 15 works as a dimensionality reduction algorithm, where the first 1D convolutional layers are dedicated to reduce the number of features initially present ($32 \times 32 \times 512$). The dimensionality reduction step is performed for each phase separately, before the remaining features are combined (simple addition in the features space). A final dense layer takes the remaining features as input and computes the probability of belonging to each class thanks to a softmax activation function (LG vs HG).

When training the network, we decided to consider that each centrally-located tumor slice of a given

patient will have a higher probability of exhibiting the highest grade, which in this case corresponds to the observed patient-wise grade (ES1954 histological grading system [2]).

Knowing the composition of TCIA-dB (9 high grade patients vs 9 low grade ones), we performed a 9-fold CV training, so that each patient is at least present once in the testing set, and so that the training and the test sets contains both the same number of patients per class (7 patients from each class in the training set and 1 patient from each class in the testing set).

After testing several combinations for the hyperparameters, we fixed the number of retained features to 8 as depicted in the figure 15 (meaning that after the features dimensionality reduction, we obtained a $32 \times 32 \times 8$ cube per phase), and we considered a 2cm volume (corresponding to 8 centrally located slices with a 2.5mm spacing) when training/testing our architecture.

With our CV-training, we were able to correctly predict the patient-wise histological grade of 15 patients among 18, as detailed in the table 2 (a patient is considered as being correctly predicted when at least half of the retained slices were annotated with the correct GT class).

When considering a slice-wise prediction, we were able to correctly predict ~74% of the slices.

Table 2: Confusion matrix regarding the patient-wise histological grade prediction

		True grade		<i>Total</i>
		LG	HG	
<i>Predicted grade</i>	LG	7	1	8
	HG	2	8	10
<i>Total</i>		9	9	18

Those results provided a more detailed prediction than the one consisting of a single patient-wise classification. Being able to compute the histological grade locally (here in a slice-wise fashion) allows us to visually focus on the heterogeneous regions that are crucial when needing to establish a diagnosis. Our pipeline can also provide a map of the best biopsy sites that will further be necessary in the clinical practice to either evaluate the progression of the disease or its prognosis.

References

- [1] Da-wei Yang, Xi-bin Jia, Yu-jie Xiao, Xiao-pei Wang, Zhen-chang Wang, and Zheng-han Yang. Noninvasive Evaluation of the Pathologic Grade of Hepatocellular Carcinoma Using MCF-3DCNN: A Pilot Study. *BioMed Research International*, 2019:1–12, apr 2019.
- [2] Steiner Edmondson HA and PE. Primary carcinoma of the liver: a study of 100 cases among 48,900 necropsies. *Cancer*, 7(3):462–503, 1954.
- [3] F. T. Bosman, F. Carneiro, R. H. Hruban, and N. D. Theise. *WHO classification of tumours of the digestive system*. Number Ed. 4. World Health Organization, Geneva, Switzerland, 2010.
- [4] Sebastiao N. Martins-Filho, Caterina Paiva, Raymundo Soares Azevedo, and Venancio Avancini Ferreira Alves. Histological grading of hepatocellular carcinoma-a systematic review of literature. *Frontiers in Medicine*, 4(NOV):1–9, 2017.
- [5] Dai Hoon Han, Gi Hong Choi, Kyung Sik Kim, Jin Sub Choi, Young Nyun Park, Seung Up Kim, Jun Yong Park, Sang Hoon Ahn, and Kwang Hyub Han. Prognostic significance of the worst grade in hepatocellular carcinoma with heterogeneous histologic grades of differentiation. *Journal of Gastroenterology and Hepatology (Australia)*, 28(8):1384–1390, 2013.
- [6] Jessica Zucman-Rossi, Augusto Villanueva, Jean Charles Nault, and Josep M. Llovet. Genetic Landscape and Biomarkers of Hepatocellular Carcinoma. *Gastroenterology*, 149(5):1226–1239.e4, 2015.
- [7] Timothy M. Pawlik, Ana L. Gleisner, Robert A. Anders, Lia Assumpcao, Warren Maley, and Michael A. Choti. Preoperative Assessment of Hepatocellular Carcinoma Tumor Grade Using Needle Biopsy. *Annals of Surgery*, 245(3):435–442, mar 2007.
- [8] Daisuke Okamoto, Kengo Yoshimitsu, Akihiro Nishie, Tsuyoshi Tajima, Yoshiki Asayama, Kousei Ishigami, Masakazu Hirakawa, Yasuhiro Ushijima, Daisuke Kakihara, Tomohiro Nakayama, Yunosuke Nishihara, Shinichi Aishima, Akinobu Taketomi, Junji Kishimoto, and Hiroshi Honda. Enhancement pattern analysis of hypervascular hepatocellular carcinoma on dynamic MR imaging with histopathological correlation: Validity of portal phase imaging for predicting tumor grade. *European Journal of Radiology*, 81(6):1116–1121, 2012.
- [9] B. B. Avants, C. L. Epstein, M. Grossman, and J. C. Gee. Symmetric diffeomorphic image registration with cross-correlation: Evaluating automated labeling of elderly and neurodegenerative brain. *Medical Image Analysis*, 12(1):26–41, feb 2008.

- [10] Farid Ouhmich, Vincent Agnus, Vincent Noblet, Fabrice Heitz, and Patrick Pessaux. Liver tissue segmentation in multiphase CT scans using cascaded convolutional neural networks. *International Journal of Computer Assisted Radiology and Surgery*, 2019.
- [11] Brian B Avants and Nick Tustison. Advanced normalization tools (ants).
- [12] Shengyu Zhao, Yue Dong, Eric I.Chao Chang, and Yan Xu. Recursive Cascaded Networks for Unsupervised Medical Image Registration. *arXiv*, pages 10600–10610, 2019.
- [13] Shengyu Zhao, Tingfung Lau, Ji Luo, Eric I.Chao Chang, and Yan Xu. Unsupervised 3D End-to-End Medical Image Registration with Volume Tweening Network. *IEEE Journal of Biomedical and Health Informatics*, 24(5):1394–1404, 2020.